communications earth & environment

Article

https://doi.org/10.1038/s43247-024-01590-6

Space-weathered rims on lunar ilmenite as an indicator for relative exposure ages of regolith

Zhuang Guo[1,2,3], Mingwei Zhang[1], Bojun Jia[1], Yang Li[2,4] ✉, Wenzhe Fa[1,4] ✉, Yong Pang[5], Chenxi Zhu[6], Yuanyun Wen[2], Xiongyao Li[2,4], Jianzhong Liu[2,4] & Ziyuan Ouyang[2]

Solar wind irradiation, as a crucial space weathering mechanism, alters the microscopic characteristics and reflectance spectrum of the lunar regolith, and its cumulative effect is strongly related to the exposure time. Ilmenite is highly resistant to solar wind irradiation. Here, we combined transmission electron microscopy, energy-dispersive X-ray spectroscopy, and electron energy loss spectroscopy to systematically illustrate the diverse space-weathered rims on the shoveled and drilled Chang'e-5 ilmenites resulting from varying degrees of solar wind irradiation, revealing that solar wind plays a key role in the early-stage alteration of exposed lunar soil. In addition, the space weathering microstructure observations are consistent with the model-predicted exposure history at the Chang'e-5 landing site and prove that the Chang'e-5 deep-layered drilled (~65 cm) and surface samples (<3 cm) have been exposed for a longer time than that of the intermediate-layered drilled samples. We conclude that the ilmenite rims have the potential to be an effective indicator for comparing the relative exposure ages of regolith on airless bodies.

The chemical and physical changes that take place to surface material by exo-dynamic processes on airless planetary bodies such as the Moon are termed "space weathering". Numerous simulation experiments and direct analyses of returned lunar material have revealed that space weathering significantly alters the physical and chemical properties of the upper tens of nanometers of minerals, thus modifying their reflectance spectrum[1,2]. Results from asteroid reflectance spectra studies suggest a key role for solar wind irradiation in the early exposure history (10^4–10^6 years) of material, while micrometeorites should act over longer timescales (10^8–10^9 years)[3]. However, space weathering rims on Apollo samples are the result of a combination of micrometeorite impacts and solar wind irradiation, and effectively distinguishing between their effects in modifying lunar material remains an unsolved problem, especially for the formation mechanisms of optically active iron particles in lunar soil[2,4–7]. One way to provide constraints on the short exposure history of lunar soil, and on the potential causes of changes in the spectra of asteroids over time, is to clarify the differences in the mineral modification characteristics and formation mechanisms of solar wind on different timescales[8,9]. Therefore, clarifying the specific modification features of lunar soils by varying degrees of solar wind irradiation is expected to establish the relationship between space weathering modification and the exposure time of lunar soils.

Ilmenite is more resistant to amorphization by ion irradiation than silicates due to its close-packed crystal structure, which has been demonstrated in previous studies[6]. Detailed microscopic analyses, including transmission electron microscopy (TEM) and atom probe tomography, suggest that space-weathered rims on lunar ilmenite grains exhibit complex chemical and structural responses to space weathering, such as the helium-bearing vesicles, structural damage, and variations of iron and titanium valence states, as compared to the amorphous rims on lunar silicates[6,10–12]. More critically, the simplicity of ilmenite elemental composition (Fe, Ti, and O) makes it easy to identify impact-induced vapor deposition on lunar soil, thus making ilmenite the most appropriate target for studying solar wind irradiation on the Moon. Therefore, the diverse space-weathered microstructures on the rim of lunar ilmenite grains could provide crucial clues to lunar soil irradiation processes under the effects of solar wind, helping us to understand the exposure history of lunar regolith.

The Chang'e-5 mission successfully recovered lunar regolith core samples at a depth of about 1 m below the lunar surface[13]. Previous studies

[1]Institute of Remote Sensing and Geographical Information System, School of Earth and Space Sciences, Peking University, Beijing, China. [2]Center for Lunar and Planetary Sciences, Institute of Geochemistry, Chinese Academy of Sciences, Guiyang, China. [3]NWU-HKU Joint Center of Earth and Planetary Sciences, Department of Geology, Northwest University, Xi'an, China. [4]Center for Excellence in Comparative Planetology, Chinese Academy of Sciences, Hefei, China. [5]Beijing Spacecrafts, Beijing, China. [6]State Key Laboratory of High Performance Ceramics and Superfine Microstructures, Shanghai Institute of Ceramics, Chinese Academy of Sciences, Shanghai, China. ✉e-mail: liyang@mail.gyig.ac.cn; wzfa@pku.edu.cn

suggest that young Chang'e-5 lunar samples were well mixed only at very shallow depths and that deeper lunar soil derived from the Xu Guangqi crater is most likely unexposed to space[14,15]. Therefore, differences in exposure times over the vertical profile of the Chang'e-5 landing site allow us to study the diverse space weathering responses of ilmenite. Here we investigate ilmenite microstructures from different depths of Chang'e-5 lunar soil to compare differences in the structural and chemical modifications on ilmenite rims under different levels of solar wind irradiation and discuss the formation mechanisms of microstructures on ilmenite surfaces in detail. In addition, we combine lunar soil evolution models and present Chang'e-5 sample observations to constrain the exposure history of Chang'e-5 lunar soils.

Results

Considering that the grain size of lunar soil is correlated with lunar regolith maturity[16], ilmenite (CE5C0200 #1) selected from the finest fraction of shoveled Chang'e-5 lunar soils (<10 μm) could represent the most space-weathered ilmenite collected by the Chang'e-5 mission (Fig. 1a). For this grain, multiple microstructures and heterogeneous chemical features appear within the top 120 nm of the FIB cross-section (Fig. 2). Specifically, quantitative TEM-EDS compositional maps and HRTEM images show that abundant elongate and spherical npFe^0 particles and large vesicles (up to 40 nm in diameter) are embedded in the almost fully amorphous Ti-rich layer of the space-weathered rim (within the top 50 nm) (Fig. 2a, b, d). The elongate-shaped iron particles are up to 60 nm in length, which is much larger than the observed spherical particles. In addition, thin planar defects were present in the partially damaged ilmenite crystal at depth (Fig. 2c).

EELS spectra show the presence of helium (diagnostic peak at about 22 eV) in large vesicles on the top surface of the ilmenite grain (Fig. 2e). The EELS spectra show the difference in the Ti valence state between the grain rim and ilmenite substrate. By comparing the spectra of the Ti^{4+} standard and ilmenite grain, the Ti $L_{2,3}$ peaks at the space-weathered rim show a low-energy shift of ~0.5 eV and a decreased splitting of the L_3 and L_2 peaks, suggesting that some Ti^{3+} should be present in the surface Ti-rich layer (Fig. 2f)[6]. The thick structural damaged rim, the production of helium-bearing vesicles, and the precipitation of large npFe^0 particles suggest that this Chang'e-5 ilmenite grain had experienced long-term exposure to solar wind irradiation.

Ilmenite-bearing lithic clasts at different depths exhibit diverse ilmenite microstructure rims. Considering that crystallographic orientation has an effect on the ion irradiation characteristics of minerals[11,17], we have classified these rims not only concerning structural damage features but also to the degree of valence changes of the elemental Fe and Ti, as well as the size of the vesicles and npFe^0 particles. Of the ten large grains examined, five groups of rims were defined based on their degree of modifications: undamaged rims (CE5C0200 #3, CE5Z0806 #1, CE5Z0403 #1 and #2, CE5Z0204 #2) (Fig. 1e and Supplementary Fig. 2), densely damaged rims (CE5Z0806 #2) (Fig. 1d), vesicular rims (CE5Z1002 #2) (Fig. 1c), npFe^0-rich rims (CE5C0200 #2, CE5Z1002 #1) (Fig. 1b and Supplementary Fig. 3), and deeply damaged rims (CE5Z0204 #1) (Fig. 1f). Each category is described in detail below, and the above-described CE5C0200 #1 grain falls into the deeply damaged rim group.

Undamaged rim. The crystallographic orientation of the undamaged rim is consistent with the substrate ilmenite and essentially no signs of solar irradiation damage are observed in the TEM images (Fig. 3a, Supplementary Fig. 2). Compared to the substrate ilmenite, quantitative energy-dispersive X-ray spectroscopy (EDS) results show only a slight depletion of elemental oxygen in the ilmenite rim (O_{rim}, 50.9 at% vs. $O_{substrate}$, 54.4 at%), and no iron-rich regions were observed (Fig. 4a1 and a2, Supplementary Table 1). In addition, the EELS data show no change in Ti *L*-edge peaks at the undamaged rim and substrate ilmenite (Figs. 4a3). Slight oxygen deficiency and the absence of structural damage are the diagnostic characteristics of the

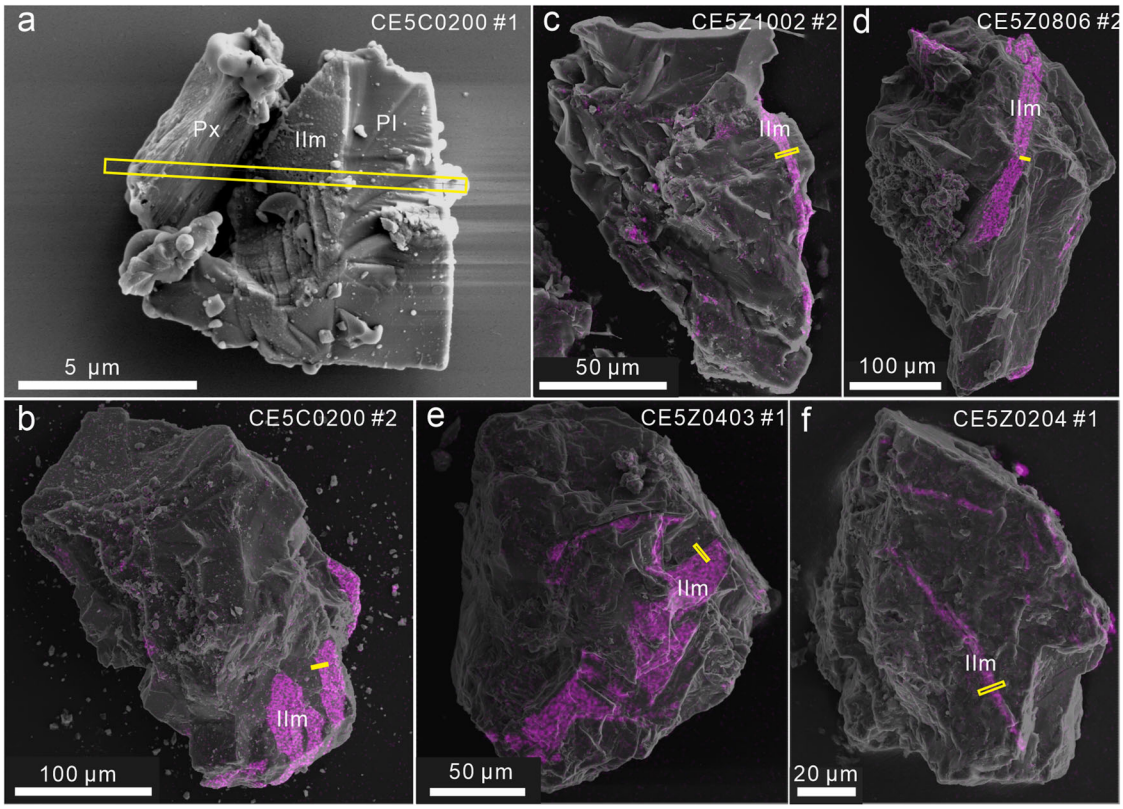

Fig. 1 | Selected ilmenite-bearing lunar grains from the shoveled and drilled Chang'e-5 samples. a The secondary electron (SE) image of the ilmenite-bearing clast from the finest shoveled Chang'e-5 lunar soil. **b–f** X-ray element maps of titanium overlaid on SE images of selected lithic clasts. Yellow rectangles indicate the extraction locations of the focused ion beam (FIB) samples.

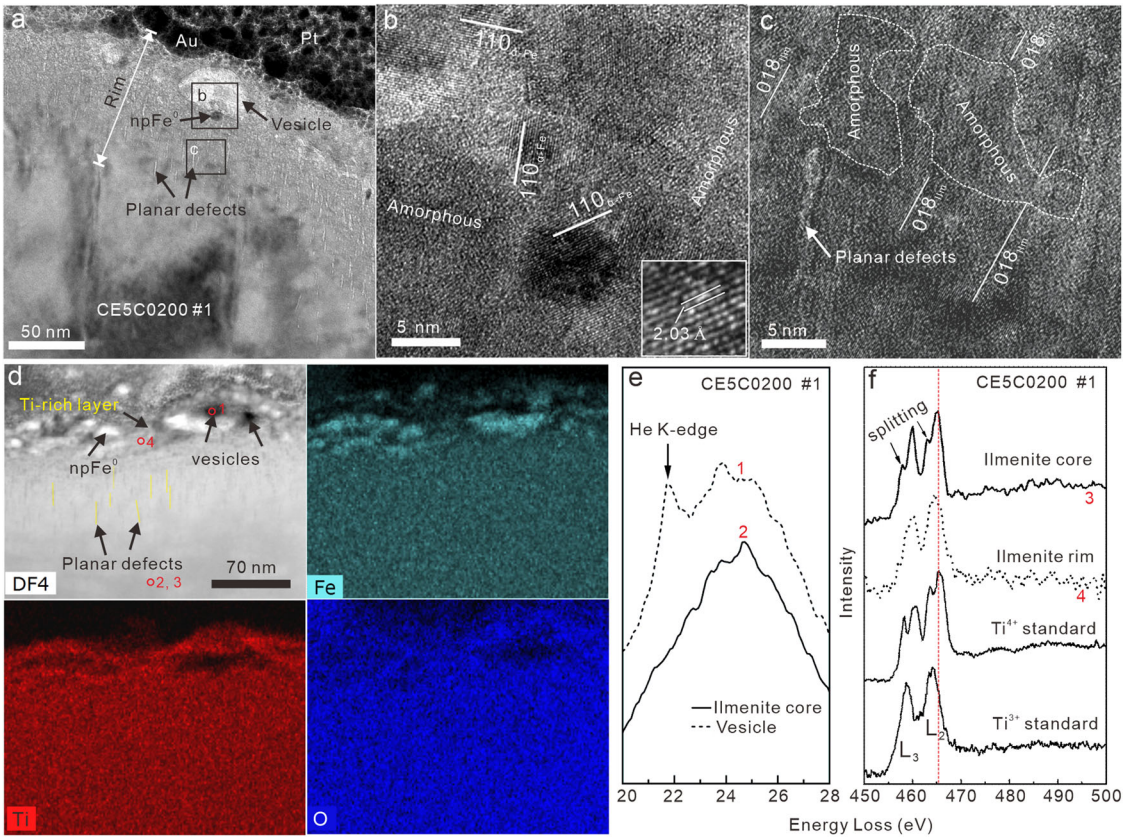

Fig. 2 | Microstructure and chemical characteristics of the CE5C0200 #1 ilmenite (Ilm) grain. a Transmission electron microscopy (TEM) bright-field image of the edge of the CE5C0200 #1 ilmenite grain. Black rectangles represent the locations of the high-resolution (HR) TEM images shown in (**b**) and (**c**). **b**, **c** HRTEM images of the outer and inner regions within the space-weathered rim, and the white lines represent the (110) and (018) lattice fringes of α-Fe and ilmenite, respectively. **d** High-angle annular dark-field (HAADF) image of the CE5C0200 #1 ilmenite rim and its corresponding quantitative energy-dispersive element maps for Fe, Ti, and O, and the red circles and numbers represent the locations of EELS spectra acquisition in (**e**) and (**f**). **e**, **f** He *K*-edge and Ti $L_{2,3}$ electron energy-loss spectra (EELS) from the substrate ilmenite and ilmenite rim in CE5C0200 #1.

undamaged rim, indicating the lowest degree of modification of the lunar soil by solar wind irradiation.

Densely damaged rim. The densely damaged rim is characterized by a planar arrangement of structural damage concentrated in the top 50 nm. Localized nano-scale structural disorder and mottled strain contrast are apparent in bright-field TEM images of the rim (Fig. 3b, Supplementary Fig. 4). Similar to the undamaged rim, oxygen depletion was also detected by EDS analysis, and the content of oxygen tended to increase with increasing distance from the surface (Supplementary Fig. 4 and Supplementary Table 1). By comparing the EELS spectra of the densely damaged rim with the Ti^{4+} standard and substrate ilmenite, the Ti $L_{2,3}$ peaks for the densely damaged rims show ~0.3 eV shifts toward low energy and decreased splitting of the L_3 and L_2 peaks, suggesting that the densely damaged rim should be a Ti^{3+}-bearing oxide (Fig. 4b3)[6,18,19]. No valence state transition of iron was observed in the densely damaged rim (Supplementary Fig. 5b)[20].

Vesicular rim. The vesicular rim shares all of the structural damage (i.e., localized nano-scale structural disorder) characteristics of the densely damaged rim. Additionally, the interior of the vesicular rim contains a large number of spherical nano-vesicles (less than 5 nm in diameter) and a few nanophase iron particles ($npFe^0$) (5–10 nm in diameter) in the top 80 nm (Figs. 3c and 4c1). In addition, trace amounts of Si enriched on the uppermost surface of the ilmenite grain were identified (Fig. 4c2). Enrichment of Ti at the vesicular rim is apparent in the quantitative EDS compositional maps, and the EELS spectra show a progressive decrease in the splitting of the Ti $L_{2,3}$ edges and a ~ 0.8 eV shift toward the low-energy Ti L_2 peak. These results suggest that oxygen loss and more Ti^{3+} production occur at the vesicular rim compared to the densely damaged rim (Fig. 4c1, c2, Supplementary Table 1). Despite the presence of a few Fe particles in the vesicular rim, no obvious characteristic broadening of the EELS Fe L_2 peak was observed for the Ti-rich matrix, indicative of the extremely low content of Fe^0 in the matrix (Supplementary Fig. 5). In addition, the EELS spectra of nano-vesicles in the vesicular rim and substrate ilmenite show no variations in energy loss within 5–30 eV (Fig. 5a). The onset of Ti-rich phases and Fe particles, as well as the numerous nano-vesicles, are additional features of the vesicular rim compared to the densely damaged rim.

$NpFe^0$-rich rim. Bright-field TEM images show that the thickness of the $npFe^0$-rich rim is about 100 nm, and this rim group can be further divided into inner and outer layers based on the distinct microstructures (Fig. 3d, Supplementary Fig. 3). The outer layer (0–40 nm) is characterized by a large number of spherical and elongated $npFe^0$ particles (~10 nm in diameter) and enlarged vesicles (up to 15 nm) embedded within the partially amorphous Ti-rich matrix and also shows the presence of Si (Figs. 4d1, d2, and 5b); only a few discontinuous lattice fringes of mineral ilmenite are observed in the outer layer (Fig. 3g). High titanium content ($Ti_{outer\ layer}$: 24.3 at% vs. $Ti_{substrate\ ilmenite}$: 22.5 at%) and oxygen deficiency ($O_{outer\ layer}$: 53.6 at% vs. $O_{substrate\ ilmenite}$: 56.8 at%) were detected in the outer layer (Fig. 4d2, Supplementary Table 1). The ubiquitous $npFe^0$ particles in the outer layer are shown as iron-rich regions in the EDS map and show a diagnostic 2.03 Å *d*-spacing of the α-Fe (Figs. 3g and 4d2, Supplementary Fig. 3d). The EELS spectra of these $npFe^0$ particles show a visible broadening of the Fe L_2 peak relative to the substrate ilmenite (Supplementary Fig. 5a). The EELS spectra of the Ti-rich phase within the outer layer also indicate the presence of the Ti^{3+} component (Fig. 4d3). In addition, the presence of helium was detected in these vesicles (>5 nm in diameter) (Fig. 5b). The inner layer (40–100 nm) has the same localized nano-scale structural disorder as the densely damaged rim, but oxygen

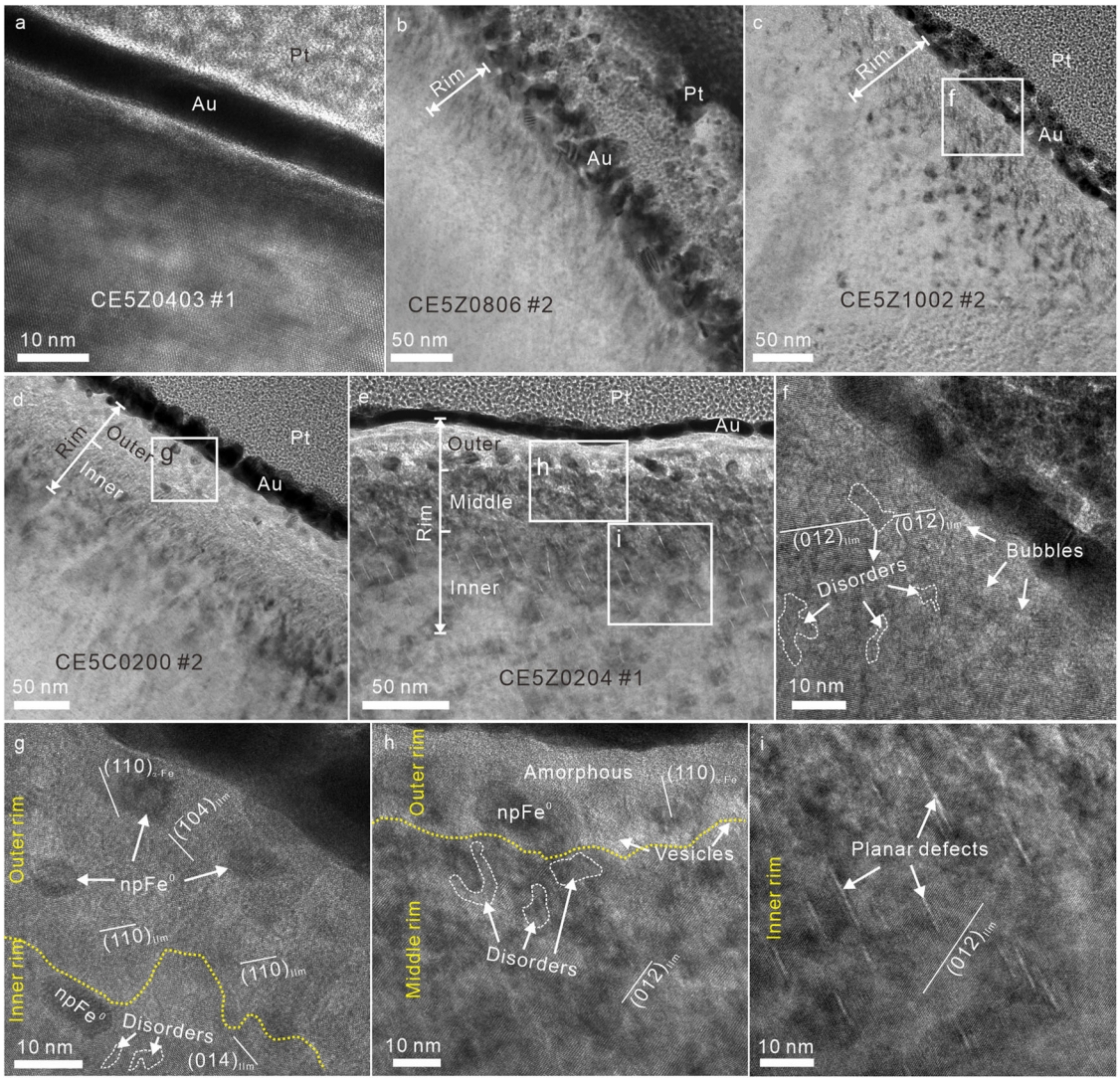

Fig. 3 | Microstructure of diverse space-weathered rims on the Chang'e-5 profiled ilmenite grains. a Transmission electron microscopy (TEM) image of the undamaged rim on the CE5Z0403 #1 ilmenite grain. **b** TEM image of the densely damaged rim on the CE5Z0806 #2 ilmenite grain. **c** The vesicular rim on the CE5Z1002 #2 ilmenite grain. **d** TEM image of the npFe^0-rich rim on the CE5C0200 #2 ilmenite grain. **e** TEM image of the deeply damaged rim on the CE5Z0204 #1 ilmenite grain. **f–i** High-resolution TEM images of those areas indicated by white rectangles in (**c**), (**d**), and (**e**). The ilmenite with vesicular rim (**f**) shows a similar crystallographic orientation with the ilmenite with deeply damaged rim ([4$\bar{2}$1] zone axis) (**h**), while the ilmenite with npFe^0-rich rims shows a [4$\bar{4}$1] zone axis (**g**).

deficiency and elemental reduction (Fe, Ti) are both absent in the inner layer (Fig. 4d3, Supplementary Fig. 5a and Supplementary Table 1).

Deeply damaged rim. The thickness of the deeply damaged rim is up to 120 nm, and the rim is further divided into outer, middle, and inner layers based on their complex microstructures. The quantitative EDS results show that oxygen deficiency is observed only in the outer layer (Supplementary Table 1). A distinct Si-rich layer (~5 nm) was observed on the surface of the ilmenite grain, which is most likely a product of impact deposition and is not related to the solar wind alteration of ilmenite, thus excluding the Si-rich layer from the classification of the three sublayers described above (Fig. 4e2). Within the top 30 nm (outer layer), the ilmenite structure is completely amorphous, in which large elongated npFe^0 (>15 nm) particles and vesicles are present (Figs. 3e, h, and 5c). The outer layer of the deeply damaged rim are thinner compared to the npFe^0-rich rims, which should be attributed to the difference in crystallographic orientation (Fig. 3g, h). The EELS spectra of the Ti-rich phase within the outer layer also indicate the presence of the Ti^{3+} component (Fig. 4e3). In addition, a clear EELS He *K*-edge peak at ~22 eV was detected in these large vesicles embedded within the outer layer (Fig. 5c). The middle layer (30–70 nm), located beneath the outer layer, shares structural characteristics of the densely damaged rim, i.e., localized nano-scale structural disorder development in the ilmenite mineral (Fig. 3h). In addition, some nano-vesicles are present in the middle layer (Fig. 3e). However, neither oxygen deficiency nor elemental reduction (Fe, Ti) was detected in the middle layer of the deeply damaged rim (Fig. 4e3, Supplementary Table 1). TEM observations show that the ubiquitous parallel thin planar defects at depth (70–120 nm) in the inner rim did not cause significant damage to the ilmenite structure, and no detectable chemical modifications were identified (Figs. 3i and 4e2).

Discussion

Solar wind irradiation response of lunar ilmenite

Based on the thickness and the microstructural complexity of the rims present in the space-weathered ilmenite surfaces, we can classify these rims from the least to the most alteration as undamaged rim, densely damaged rim, vesicular rim, npFe^0-rich rim, and deeply damaged rim. Vapor deposit layers are widely distributed on the exposed surfaces of lunar soil and always exhibit elemental Si enrichment[21]. Therefore, the exotic Si compositions detected in the intermediate (vesicular rim) and highly weathered (npFe^0-rich rim and deeply damaged rim) ilmenite grains also suggest that these grains have experienced a long-term space exposure (Fig. 4c2, d2, e2). By

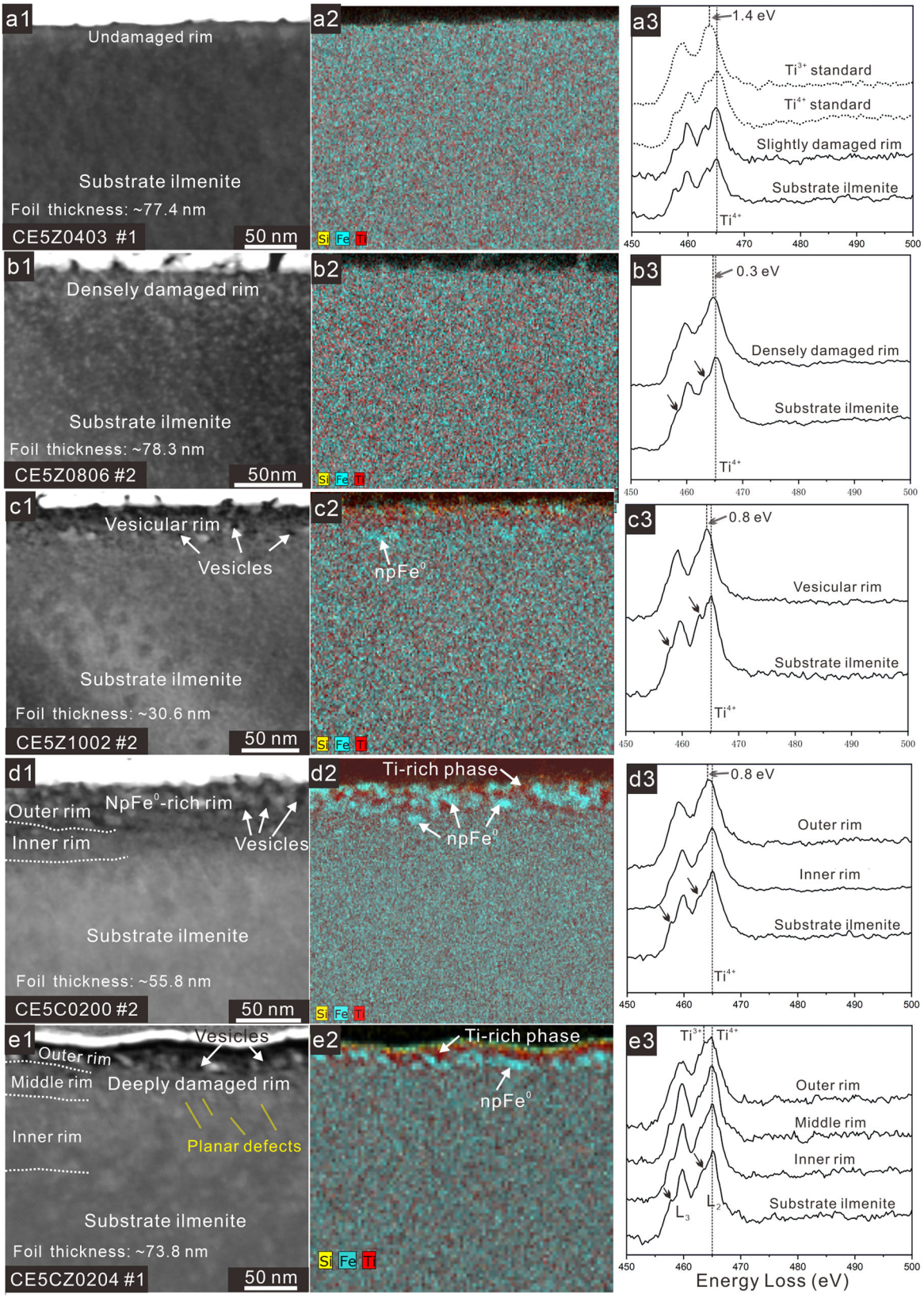

Fig. 4 | Chemical characteristics of diverse space-weathered rims on the Chang'e-5 profiled ilmenite grains. a–e High-angle annular dark-field (HAADF) images (**a1**–**e1**) and their corresponding quantitative energy-dispersive X-ray spectroscopy (EDS) element maps (**a2**–**e2**), together with Ti $L_{2,3}$ EELS spectra (**a3**–**e3**), respectively. The included Si element in the EDS maps is to distinguish the presence of exogenous vapor deposited material on the ilmenite surfaces. The arrows in the EELS spectra (**a3**–**e3**) represent the splitting of the Ti $L_{2,3}$ peaks, and the decrease in splitting correlates with the presence of Ti^{3+}.

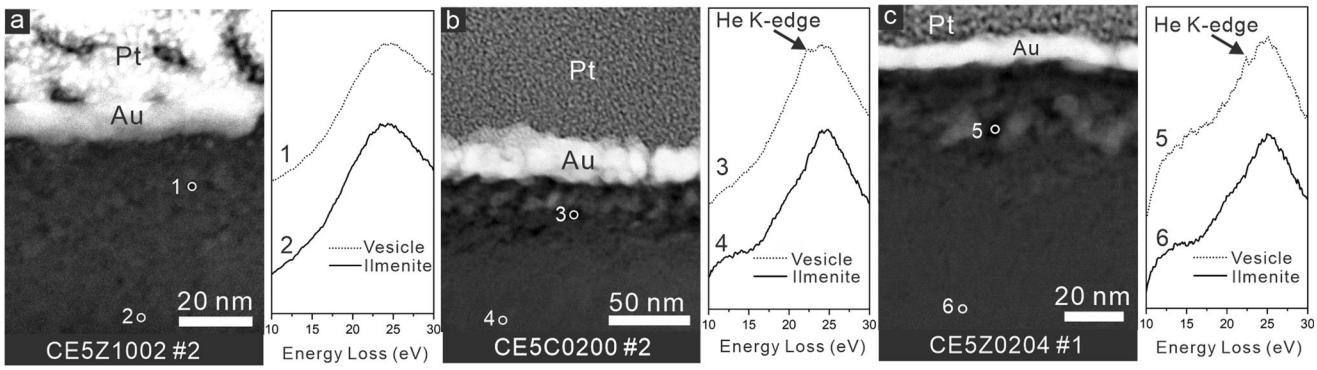

Fig. 5 | He K-edge EELS spectra in the vesicles of the diverse rims on Chang'e-5 profiled ilmenite grains. a He K-edge EELS spectra from the substrate ilmenite and nano-vesicles of the vesicular rim on the CE5Z1002 #2 ilmenite grain. **b**, **c** He K-edge EELS spectra from the substrate ilmenite and large vesicles in the highly weathered ilmenite rims (i.e., the npFe^0-rich rim and the deeply damaged rim) on the CE5C0200 #2 and CE5Z0204 #1 ilmenite grains, respectively.

comparing previous in-situ ion irradiation experiments and analyses of lunar soils, we could attribute specific characteristics in these Chang'e-5 ilmenite grains to different degrees of solar wind irradiation on the lunar surface.

Structural damage (e.g., amorphization and crystal defects) to materials caused by solar wind irradiation has been confirmed by ion irradiated simulation experiments[22–24]. The structural damage is concentrated on the surface of Chang'e-5 ilmenite, and its depth range (100–200 nm) coincides exactly with the results of energetic particle irradiation under simulated lunar conditions[10,25]. In addition, solar wind components (H or He) have been detected in the planar defects of Apollo ilmenite space-weathered rims, thus the solar wind ion implantation is the main cause of such planar defects[11,12]. In the Chang'e-5 ilmenite grains, the early-stage structural damage appears as localized nano-scale structural disorder in the most superficial layer (~50 nm), and with the accumulation of solar wind irradiation, the superficial layer becomes amorphous, and the structural disorder and planar defects appear at a greater depth (up to 120 nm).

The "nano-vesicles" occur in the intermediate stage of lunar ilmenite weathering, the formation of these "nano-vesicles" in the vesicle rim is likely to be the result of the cumulative effect of solar wind irradiation to saturation fluence[26–28]. It is well known that prolonged irradiation with a high ion fluence can result in the formation of voids on the surfaces of many materials[29]. Although no helium signals were detected in these "nano-vesicles", solar wind implantation should not be completely excluded, as their content in individual nano-vesicles may be very low. Given that the large vesicles take a sufficiently long time to nucleate and may coalesce from smaller bubbles during heating, and that helium trapping is confirmed by large vesicles in the space-weathered ilmenite rims from Apollo and Chang'e-5 lunar soils[11,27,30]. Therefore, it is most likely that large helium-bearing vesicles in the npFe^0-rich and deeply damaged ilmenite rims should have developed from these precursor "nano-vesicles" observed in the vesicular rim at a temperature condition of <400 °C (to avoid the solar wind gases release)[11,27,31,32].

In addition to structural changes, oxygen deficiency and elemental Fe-Ti reduction are the most pronounced chemical alteration at the weathered ilmenite rims. It is observed that the reduction of elements and the loss of oxygen occurs only in the uppermost surfaces of space-weathered ilmenite (<40 nm), while the inner layers (i.e., middle and inner layers of the deeply damaged rim, and inner layer of the npFe^0-rich rim) are devoid of these features, implying that the loss of oxygen during solar wind irradiation is mainly by sputtering and provides important conditions for the reduction of Fe and Ti (Fig. 4 and Supplementary Fig. 7)[10,19,33,34]. Combined with the solar wind-dominated effects on microstructures (e.g., structural damage and vesicle formation), we conclude that superficial oxygen loss and the Ti reduction in space-weathered ilmenite rims are also primarily controlled by solar wind irradiation. However, there has been controversy about the formation of iron particles as a direct result of the solar wind, and a combination of solar irradiation and post-subsolidus heating effects was invoked to explain the npFe^0 particle in-situ formation[6,19]. There are several possible post-heating scenarios for the formation and growth of npFe^0 particles, such as micro-impact events or solar thermal radiation. However, no significant indigenous npFe^0 particles derived from the host ilmenite were observed within impact-induced micro-crater on a Chang'e-5 ilmenite grain (Supplementary Fig. 8). In addition, our observations show that large helium-bearing vesicles form simultaneously with abundant npFe^0 particles in highly space-weathered ilmenite rims. Considering that solar-wind implanted noble gases are easily released under high-temperature conditions (>400 °C), the formation of npFe^0 particles and the growth of vesicles at the space-weathered ilmenite rims should be subject to a low-temperature post-heating condition[27,35]. Previous studies have proposed that a long-term thermal process provided by diurnal solar heating (100–120 °C) may promote the formation of npFe^0 particles and large vesicles within the 40 nm thickness range on the ilmenite surface by radiation-enhanced diffusion[6]. All these observations suggest that solar wind plays a key role in the early-stage structural and chemical changes of airless material exposed to space.

The exposure history of Chang'e-5 lunar soils

Based on remote sensing observations and ejecta deposition models, the Xu Guangqi crater (<100 Myr) ejecta is the main contributor to the Chang'e-5 samples[15]. Therefore, the thickness of the ejecta from Xu Guangqi crater is critical to tracking the provenance of samples recovered from different depths at the Chang'e-5 landing site. A crater ejecta thickness distribution model was used to estimate the ejecta thickness from Xu Guangqi crater at the Chang'e-5 landing site, with resulting estimates of 29.8 cm[36]. In addition, 11 smaller impact craters (C2–C12) surrounding the Chang'e-5 landing site cumulatively ejected a deposit ~18.9 cm-thick of ejecta over approximately 100 Myr after the Xu Guangqi ejecta emplacement[36]. Therefore, the results of the ejecta deposition model indicate that the cumulative thickness of ejecta at the Chang'e-5 landing site should not exceed 48.7 cm over the past 100 Myr. The regolith overturn model shows that the overturning of lunar soil occurred at a depth of no more than 20 cm within 100 Myr after the emplacement of Xu Guangqi ejecta, suggesting that the material from Xu Guangqi crater situated >20 cm depth was most likely not exposed to the space environment[15,37]. In addition, there are multiple sources of the uppermost lunar regolith (<20 cm), including Xu Guangqi ejecta and fresh impact craters inside and outside the P58 unit[15]. Therefore, the Chang'e-5 lunar soils collected from the uppermost surface layer (<20 cm) should exhibit highly variable exposure times[38].

We combined ground-penetrating radar data from the Chang'e-5 landing site and corrected the slip of the lunar soil during sampling to obtain the actual depths of the drilled samples (CE5Z1002, 0–2 cm; CE5Z0806, ~26 cm; CE5Z0403, ~45 cm; CE5Z0204, 65–72 cm)[39] (Supplementary Fig. 1). Combined with theoretical model predictions, the drill sample from CE5Z0204 recovered at 65–72 cm is likely derived from the regolith material

that predates the formation of the Xu Guangqi crater and underwent long-term exposure[15,40,41]. The most space-weathered ilmenite grain (deeply damaged rim) was identified from the CE5Z0204 lunar soil, suggesting that lunar soil depths greater than 65 cm must have experienced a relatively long exposure history (Fig. 6). In addition, overturning processes within the past 100 Myr would not have exposed lunar soil at this depth to the surface. Therefore, our observations are consistent with model predictions that a pre-Xu Guangqi ancient regolith layer exists below 65 cm depth at the Chang'e-5 landing site. Weakly weathered ilmenite grain (CE5Z0204 #2) was also found in the deep-drilled CE5Z0204 lunar soil, reflecting the possible presence of ejecta from the then-newly formed impact craters during the formation and evolution of the pre-Xu Guangqi ancient regolith. The result implies that unexposed grains may be present at any depth of the lunar regolith, but the presence of highly space-weathered grains should indicate that the lunar regolith has experienced long-term exposure.

Referring to the model results, drilled samples of CE5Z0403 (45 cm) and CE5Z0806 (26 cm) are predominantly ejecta deposits from Xu Guangqi, and these fractions of lunar soil were likely unaffected by the subsequent 100 Myr of overturning to reach the lunar surface and experience exposure to space. Our observations show that ilmenite grains from lunar soils CE5Z0403 and CE5Z0806 are generally characterized by a low degree of space weathering, supporting that these two lunar soils are unexposed ejecta deposits derived from Xu Guangqi crater (Fig. 6).

The CE5C0200 and CE5Z1002 lunar samples were collected within 0–3 cm below the surface, and lunar soils at this depth likely overturned more than 1000 times since the formation of the Xu Guangqi crater. Moreover, the model results indicate that the provenance of the lunar soil on the surface is complex, containing Xu Guangqi ejecta, bedrock clasts excavated from fresh impact craters (C2–C12), and possible trace amounts of distal ejecta from large impact craters[15]. Therefore, the exposure history of the lunar soil in the surface regolith at the Chang'e-5 landing site is heterogeneous. Our observations show that ilmenite grains from CE5C0200 and CE5Z1002 in the superficial lunar soil exhibit a variety of weathering degrees: weakly (CE5C0200 #3), intermediate (CE5Z1002 #2), and highly weathered ilmenite (CE5Z1002 #1, CE5C0200 #1, and #2).

Our results show that the Chang'e-5 mission successfully sampled the ancient regolith material beneath the lower Xu Guangqi ejecta, and constrained the lower boundary of the Xu Guangqi ejecta at the Chang'e-5 landing site (65 cm depth or less)[15]. It is worth noting that our study involves only a very small number of lunar soil grains, and the exposure history of the lunar soil layer at each depth is likely very heterogeneous. General observations of less weathered ilmenite grains in CE5Z0403 and CE5Z0806 can only provide evidence that regolith at depths of 26 cm and 45 cm at the Chang'e-5 landing site was likely were exposed for a short period. The reflectance spectral results of the Chang'e-5 subsurface soils also show fresher spectral features compared to the surficial soils[42], which supports the possibility that the intermediate layer of the Chang'e-5 landing site has only experienced weak exposure.

Overall, ilmenites from different depths at the Chang'e-5 landing site were studied to characterize the specific features of the lunar material irradiated by different degrees of space weathering. The progressive microstructural and chemical changes occurring on the ilmenite surface indicate that solar wind plays a key role in the early-stage alteration of exposed lunar soil. Referring to the crater ejecta deposition and lunar regolith overturn model results, sample observations are consistent with the model-predicted exposure history of Chang'e-5 lunar soil. Given the fast saturation rate of the solar wind (less than a few thousand years), we conclude that the varying degrees of space-weathered microstructures of ilmenite are useful indicators for assessing the short-term exposure history of lunar and asteroid soils. Many indices have been proposed in the last decades to estimate the exposure time of lunar soils, such as agglutinate content, Is/FeO parameter, noble gas contents, and the solar flare track density[25], and our study is an alternative approach to identifying soil exposures for cases where only a small amount of samples are returned, from deep lunar regolith or asteroids.

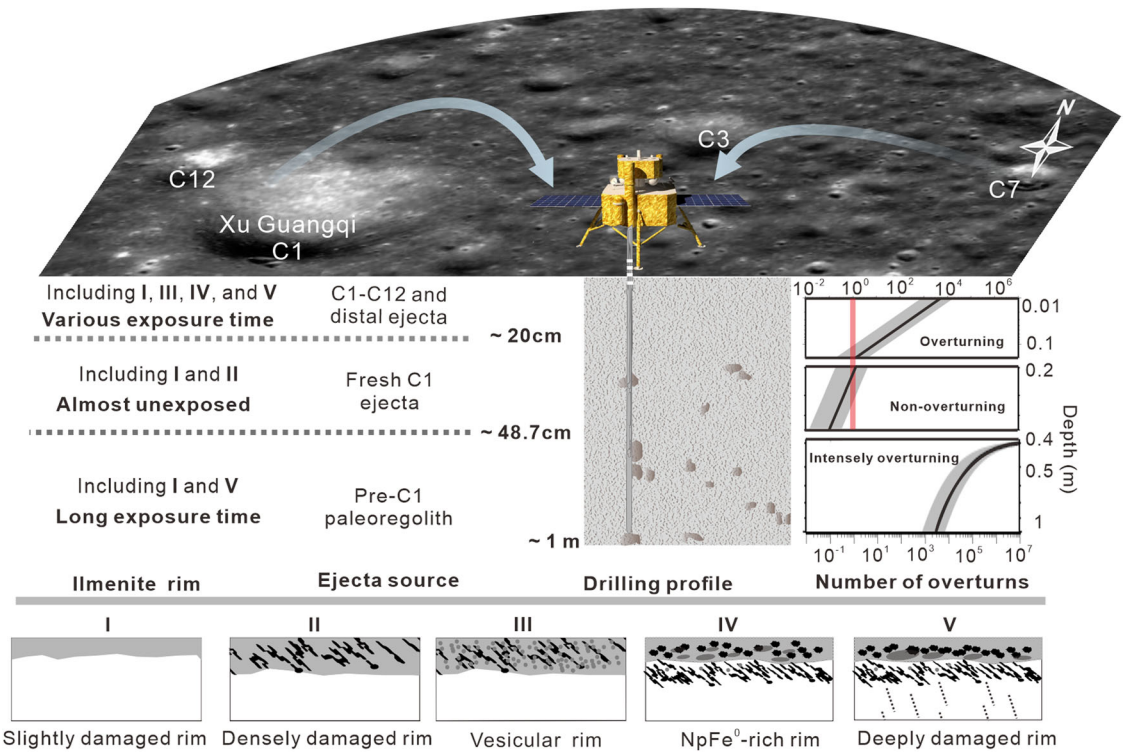

Fig. 6 | Schematic of exposure history depth profiles of Chang'e-5 lunar soil. The description in the left column represents the microscopic observations of Chang'e-5 ilmenite grains from different depth profiles, and the right column is the overturn model results of the depth profile of the Chang'e-5 landing site[15]. The ejecta source and Drilling profile columns are referenced from previous studies[15,39].

Samples and methods

The studied Chang'e-5 lunar soils are labeled from the lunar surface to the depth in the following order: CE5C0200 (shoveled), CE5Z1002 (drilling), CE5Z0806 (drilling), CE5Z0403 (drilling) and CE5Z0204 (drilling) (Supplementary Fig. 1). Lunar soil grains larger than 100 microns were placed on top of a scanning electron microscope (SEM) stub with a carbon substrate and coated with a thin layer of gold film for SEM observations. The finest-grained shoveled Chang'e-5 soil was dispersed onto a gold-plated silicon wafer using ≥99.8% high-purity ethanol, then the sample was covered with a gold film for SEM observations, and the CE5C0200 #1 grain (~10 μm) was selected in this sample for studying the most space-weathered ilmenite.

Eleven Chang'e-5 ilmenite-bearing lithic clasts (CE5C0200 #1, #2 and #3; CE5Z1002 #1 and #2; CE5Z0806 #1 and #2; CE5Z0403 #1, #2; CE50204 #1, #2) were initially selected in BSE imaging and further characterized by energy-dispersive X-ray spectroscopy (EDS) using an FEI Scios field-emission SEM housed in the Institute of Geochemistry, Chinese Academy of Sciences (CAS) (Fig. 1, Supplementary Fig. 2 and Fig. 3). Cross sections of ilmenite grains from different depths of the Chang'e-5 landing site were prepared by the focused ion beam (FIB). We extracted FIB slices that cut across the long-axis of plate-like ilmenite grains (Fig. 1 and Supplementary Fig. 2), trying to have all FIB slices from the same crystallographic orientation of ilmenite. FIB sections were characterized by a FEI Talos F200X field-emission scanning transmission electron microscope (FE-STEM) operating at 200 kV, at the Suzhou Institute of Nano-tech and Nano-bionics, CAS. STEM images were collected in high-angle annular dark field (HAADF) mode, with a 0.16 nm probe. Chemical analysis of FIB sections, including X-ray elemental mapping and EDS spectral acquisition, was performed using the silicon drift detector (SDD)-EDS on the Talos F200X instrument. TEM-EDS maps were quantified using the Cliff-Lorimer ratio technique with standard k-factors in Bruker Esprit software for the Talos[43], and data in Supplementary Table 1 are based on area selections from the quantitative TEM-EDS maps. High-resolution TEM images and selected area electron diffraction patterns (SAED) were acquired to identify the structure of minerals in the FIB sections.

Electron energy loss spectroscopy (EELS) was used to calculate the thickness of FIB cross sections and characterize the elemental valence states of iron and titanium as well as the helium within vesicles in the Chang'e-5 ilmenite rims. EELS analyses of FIB sections were performed using a Gatan GIF Quantum ER System Model 965 parallel EELS spectrometer, attached to a Hitachi HF5000 aberration-corrected scanning transmission electron microscope, operating at an accelerating voltage of 200 kV with a 0.078 nm probe diameter, which is housed at the Shanghai Institute of Ceramics, CAS. EELS spectrum images (SI) were acquired in DualEELS mode with a probe current of 100 pA. The energy dispersion for EELS measurements was 0.1 eV/channel with an energy resolution was ~0.5 eV, measured from the full width at half the maximum height of the zero-loss peak. The relative thickness (t/λ) of FIB films was calculated based on the equation of $\frac{t}{\lambda} = \ln\frac{I}{I_0}$, where t is the absolute thickness of the FIB films, λ electron mean-free-path, and I is the total integrated area under the EELS spectrum and I_0 is the area under the zero-loss peak (ZLP). The relative thickness (t/λ) of these studied FIB films was extracted from their EELS ZLP spectra using the Gatan Microscopy Suite (GMS) software, with values ranging from 0.34 to 0.87. Additionally, the λ value of the $FeTiO_3$ was calculated to be approximately 90 nm by using the Mean Free Path Estimator of DigitalMicrograph script (available at http://www.dmscripting.com/meanfreepathestimator.html). Therefore, the absolute thickness (t) of these studied FIB films was determined to be 30.6–78.3 nm. EELS integration times were 8.8 s for Fe point analyses, 26.4 s for Fe analyses at each point in the line-scan, 1 s for He point analyses, 10 s for line-scans of Ti at each point, and 17.6 s for Ti analyses at each point in the line-scan. The synthetic Ti_2O_3, rutile (TiO_2), fayalite, terrestrial hematite, and FeNi metal from meteorite (GRV 051874) were prepared as Ti^{3+}, Ti^{4+}, Fe^{2+}, Fe^{3+}, and Fe^0 reference standards for the comparing valence transition in the space-weathered ilmenite rims (Supplementary Fig. 6). Peak alignment to compensate for energy drift during EELS SI acquisition and the background subtracted by power law were carried out using Gatan Digital Micrograph software.

Details of crater ejecta thickness distribution and overturn modeling are available in Text 1 in Supplementary Information, and these models were run in Python.

Data availability

The original TEM images, EELS data, and FIB foil thickness results used in this work are publicly available online (https://figshare.com/s/f67768f7856487675aed).

Received: 9 January 2024; Accepted: 30 July 2024;
Published online: 12 August 2024

References

1. Hapke, B. Space weathering from Mercury to the asteroid belt. *J. Geophys. Res. Planets* **106**, 10039–10073 (2001).
2. Pieters, C. M. & Noble, S. K. Space weathering on airless bodies. *J. Geophys. Res. Planets* **121**, 1865–1884 (2016).
3. Vernazza, P., Binzel, R., Rossi, A., Fulchignoni, M. & Birlan, M. Solar wind as the origin of rapid reddening of asteroid surfaces. *Nature* **458**, 993–995 (2009).
4. Housley, R., Cirlin, E., Paton, N. & Goldberg, I. Solar wind and micrometeorite alteration of the lunar regolith. *Lunar Sci. Conf.* **5**, 2623–2642 (1974).
5. Keller, L. P. & McKay, D. S. The nature and origin of rims on lunar soil grains. *Geochim. Cosmochim. Acta* **61**, 2331–2341 (1997).
6. Christoffersen, R., McKay, D. S. & Keller, L. P. Microstructure, chemistry, and origin of grain rims on ilmenite from the lunar soil finest fraction. *Meteorit. Planet. Sci.* **31**, 835–848 (1996).
7. Denevi, B. W. et al. Space weathering at the Moon. *Rev. Mineral. Geochem.* **89**, 611–650 (2023).
8. Noguchi, T. et al. Incipient space weathering observed on the surface of Itokawa dust particles. *Science* **333**, 1121–1125 (2011).
9. Hiroi, T. et al. Evidence of global space weathering by solar wind on asteroid 162173 Ryugu. *Icarus* **406**, 115755 (2023).
10. Christoffersen, R., Keller, L. P., Dukes, C., Rahman, Z. & Baragiola, R. Experimental investigation of space radiation processing in lunar soil ilmenite: combining perspectives from surface science and transmission electron microscopy. In *Lunar Planet. Sci. Conf.* **41**, 1532 (2010).
11. Burgess, K. D. & Stroud, R. M. Phase-dependent space weathering effects and spectroscopic identification of retained helium in a lunar soil grain. *Geochim. Cosmochim. Acta* **224**, 64–79 (2018).
12. Greer, J. et al. Atom probe tomography of space-weathered lunar ilmenite grain surfaces. *Meteorit. Planet. Sci.* **55**, 426–440 (2020).
13. Zheng, Y. et al. Analysis of Chang'e-5 lunar core drilling process. *ChJA* **36**, 292–303 (2023).
14. Li, J. et al. Weak influence of the secondary surface processes on the regolith of Chang'E-5 landing site. *Commun. Earth Environ.* **4**, 278 (2023).
15. Jia, B. et al. On the provenance of the Chang'E-5 lunar samples. *Earth Planet. Sci. Lett.* **596**, 117791 (2022).
16. Noble, S. K. et al. The optical properties of the finest fraction of lunar soil: Implications for space weathering. *Meteorit. Planet. Sci.* **36**, 31–42 (2001).
17. Li, Y. et al. Crystal orientation results in different amorphization of olivine during solar wind implantation. *J. Geophys. Res. Planets* **118**, 1974–1982 (2013).
18. Stoyanov, E., Langenhorst, F. & Steinle-Neumann, G. The effect of valence state and site geometry on Ti L 3, 2 and OK electron energy-loss spectra of TixOy phases. *Am. Mineral.* **92**, 577–586 (2007).
19. Zhang, S. & Keller, L. A STEM-EELS study of the effect of solar-wind irradiation on the ilmenite from lunar soil. *Microsc. Microanal.* **16**, 1216–1217 (2010).

20. Garvie, L. A. & Buseck, P. R. Ratios of ferrous to ferric iron from nanometre-sized areas in minerals. *Nature* **396**, 667–670 (1998).
21. Gu, L. et al. Space weathering of the Chang'e-5 lunar sample from a mid-high latitude region on the moon. *Geophys. Res. Lett.* **49**, e2022GL097875 (2022).
22. Loeffler, M., Dukes, C. & Baragiola, R. Irradiation of olivine by 4 keV He^+: Simulation of space weathering by the solar wind. *J. Geophys. Res. Planets* **114**, E03003 (2009).
23. Christoffersen, R. & Keller, L. Space plasma ion processing of ilmenite in the lunar soil: insights from in-situ TEM ion irradiation experiments. In *Lunar Planet. Sci. Conf.* **38**, 1969 (2007).
24. Chaves, L. et al. Evaluating the effects of space weathering on magnetite on airless planetary bodies. *Icarus* **402**, 115634 (2023).
25. Keller, L. P., Berger, E. L., Zhang, S. & Christoffersen, R. Solar energetic particle tracks in lunar samples: a transmission electron microscope calibration and implications for lunar space weathering. *Meteorit. Planet. Sci.* **56**, 1685–1707 (2021).
26. Demyk, K. et al. Structural and chemical alteration of crystalline olivine under low energy He^+ irradiation. *Astron. Astrophys.* **368**, L38–L41 (2001).
27. Futagami, T., Ozima, M., Nagal, S. & Aoki, Y. Experiments on thermal release of implanted noble gases from minerals and their implications for noble gases in lunar soil grains. *Geochim. Cosmochim. Acta* **57**, 3177–3194 (1993).
28. Trinkaus, H. Energetics and formation kinetics of helium bubbles in metals. *RadEf* **78**, 189–211 (1983).
29. Clinard, F. Jr & Farnum, E. Irradiation effects in ceramics: transition from low to high dose behavior. *JNuM* **206**, 353–359 (1993).
30. Li, A. et al. Taking advantage of glass: capturing and retaining the helium gas on the moon. *Mater. Futures* **1**, 035101 (2022).
31. Nichols, R. Jr, Hohenberg, C. & Olinger, C. Implanted solar helium, neon, and argon in individual lunar ilmenite grains: surface effects and a temporal variation in the solar wind composition. *Geochim. Cosmochim. Acta* **58**, 1031–1042 (1994).
32. Scherzer, B. M. Development of surface topography due to gas ion implantation. *Sputtering by Particle Bombardment II: Sputtering of Alloys and Compounds, Electron and Neutron Sputtering, Surface Topography*, 271–355 (2005).
33. Burke, D. et al. Solar wind contribution to surficial lunar water: laboratory investigations. *Icarus* **211**, 1082–1088 (2011).
34. Zhu, Y. et al. Mineral surface modification induced by low energy ion irradiation: Implications for solar-wind exposure effects in lunar soil. *Chin. J. Geochem.* **33**, 351–356 (2014).
35. Becker, R. H. & Pepin, R. O. Long-term changes in solar wind elemental and isotopic ratios: a comparison of two lunar ilmenites of different antiquities. *Geochim. Cosmochim. Acta* **53**, 1135–1146 (1989).
36. Sharpton, V. L. Outcrops on lunar crater rims: Implications for rim construction mechanisms, ejecta volumes and excavation depths. *J. Geophys. Res. Planets* **119**, 154–168 (2014).
37. Huang, Y. H. et al. Heterogeneous impact transport on the Moon. *J. Geophys. Res. Planets* **122**, 1158–1180 (2017).
38. Zhang, M., Fa, W. & Eke, V. R. Modeling the Evolution of Lunar Regolith: 1. Formation mechanism through individual simple impact craters. *J. Geophys. Res. Planets* **128**, e2023JE007850 (2023).
39. Su, Y. et al. Hyperfine structure of regolith unveiled by Chang'E-5 lunar regolith penetrating radar. *ITGRS* **60**, 1–14 (2022).
40. Jia, B., Fa, W., Xie, M., Tai, Y. & Liu, X. Regolith properties in the Chang'E-5 landing region of the moon: results from multi-source remote sensing observations. *J. Geophys. Res. Planets* **126**, e2021JE006934 (2021).
41. Li, Q.-L. et al. Two-billion-year-old volcanism on the Moon from Chang'e-5 basalts. *Nature* **600**, 54–58 (2021).
42. Wu, Y. et al. Visible and near-infrared spectral results of Chang'E-5 surficial and subsurface soils. *Astron. Astrophys.* **682**, A112 (2024).
43. Cliff, G. & Lorimer, G. W. The quantitative analysis of thin specimens. *JMic* **103**, 203–207 (1975).

Acknowledgements

We thank CNSA for providing access to the Chang'e-5 lunar soils. We also thank K. Burgess, B. Cymes, and L. Chaves reviewer for their constructive comments on the manuscript and Dr. Chang Lu from Gatan China for his help in calculating the sample thicknesses from the EELS data. The authors acknowledge funding from the Natural Science Foundation of China (grant number 42303039, 41941002), the Strategic Priority Research Program of the Chinese Academy of Sciences (grant XDB 41000000), the "from 0 to 1" Original Innovation & Exploration Cultivation Project, Institute of Geochemistry, Chinese Academy of Sciences (DHSZZ2023-3), the China Postdoctoral Science Foundation (2023T160006), and the Key Project of Shaanxi Provincial Natural Science Basic Research Program (grant number 2023-JC-ZD-16).

Author contributions

Z.G. contributed to the conception, methodology, investigation, and paper writing of this study. M.Z. and B.J. contributed to the methodology and paper writing. Y.L. and W.F. were responsible for the supervision, and paper revision. Y.P., C.Z., and Y.W. contributed to the methodology and investigation. X.L., J.L., and Z.O. contributed to the funding acquisition.

Competing interests

The authors declare no competing interests.

Additional information

Supplementary information The online version contains supplementary material available at https://doi.org/10.1038/s43247-024-01590-6.

Correspondence and requests for materials should be addressed to Yang Li or Wenzhe Fa.

Peer review information *Communications Earth & Environment* thanks Brittany Cymes, Laura Chaves and Katherine Burgess for their contribution to the peer review of this work. Primary Handling Editors: Candice Bedford, Joe Aslin, Martina Grecequet and Carolina Ortiz Guerrero. A peer review file is available.